Effects of the adjustable ring-mode laser on intermetallic formation and mechanical properties of steel to aluminium laser welded lap joints

S. Jabar [a,*], A. Baghbani Barenji [a], P. Franciosa [a], H.R. Kotadia [a,b], D. Ceglarek [a]

[a] WMG, University of Warwick, Coventry CV4 7AL, UK
[b] School of Engineering, Liverpool John Moores University, Liverpool L3 3AF, UK

HIGHLIGHTS

- A maximum lap-shear strength of 97.6 N/mm^2 was achieved with a ring-dominant setup in conduction mode welding.
- In conduction mode, the ring-dominant beam suppressed the total intermetallic thickness and increased the weld width.
- In keyhole mode, with a ring-dominant beam, significant grain refinement was observed in the steel-side of the weld.

GRAPHICAL ABSTRACT
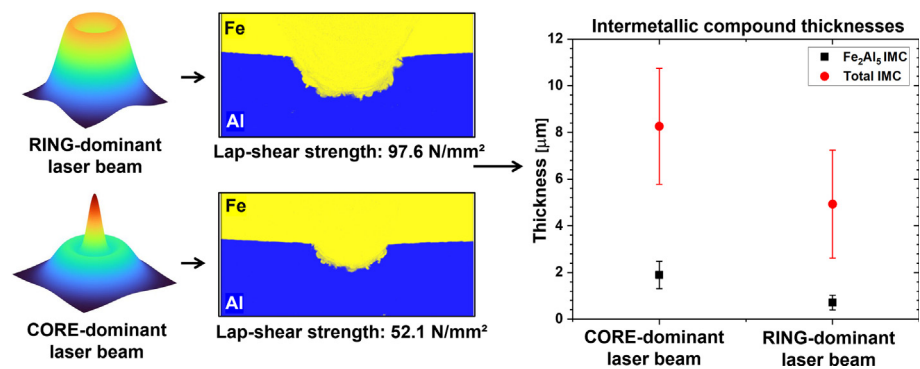
ABSTRACT

Research has confirmed a positive effect of laser beam shaping on controlling weld profiles and keyhole stabilisation, with significant reductions of porosity in weldments. However, few attempts with scattered results have studied the impact of laser beam shaping on intermetallic phase formation. This paper implements the adjustable-ring mode (ARM) laser and studies the impact of the core/ring power ratio to explore the impact on intermetallic phase formation and mechanical properties during remote laser welding of IF steel to 1050 aluminium. It was found that in conduction mode, the core/ring power ratio of 0.2 provided a larger surface area for bonding at the weld interface, and this was translated through the maximum lap-shear strength of 97.6 N/mm^2 (joint efficiency 71%). Furthermore, this significantly reduced the Fe_2Al_5 intermetallic compound (IMC) thickness by 62% and total IMC thickness by 40% in contrast to a core-dominant beam (power ratio greater than one). In keyhole mode, cracking and lower lap-shear strengths were observed compared to the conduction mode. Notably, with a core/ring power ratio of 0.5 a significant grain refinement in the steel side of the weld was observed.

1. Introduction

There are a large variety of industries that require dissimilar materials to be joined for chemical, structural and economic reasons. This includes lightweight industrial machineries, automotive body construction [1] and manufacturing of battery packs and e-drives for electric powertrains [2]. The main driving force is the possibility to complement the properties of dissimilar metals and develop functionally efficient structures [3]. In particular, the joining of steel and aluminium has gained a lot of attention in many sectors, thanks to the low density, high specific strength, corrosion resistance and good electrical properties of aluminium and the

high-strength and creep resistance of steel [4]. However, when joining steel to aluminium the reaction between iron (Fe) and aluminium (Al) atoms during the joining process forms brittle intermetallic compounds (IMCs). The mechanical strength of the joint is limited by the presence of these IMCs and therefore the amount of these compounds should be controlled. IMCs form at the Fe-Al weld interface and consist mainly of FeAl, FeAl$_3$, FeAl$_2$, Fe$_2$Al$_5$ and Fe$_4$Al$_{13}$ layers [5,6]. It is widely recognised that the total thickness of the IMC layer must be minimised, but simultaneously the formation of an IMC layer is necessary for the creation of a metallurgical bond at the Fe-Al interface. Previous research confirmed that a total and uniform IMC thickness less than 10 μm is sufficient to achieve a joint efficiency of approximate 77% compared to the strength of aluminium [7,8]. These IMCs form due to the poor solubility of Fe into Al which can compromise the mechanical performance of the weld if in excessive amounts. IMCs possess distinctive properties, such as hardness, limited ductility and toughness and morphology [6,9,10]. The recent published work in [5,6] found that the Fe$_2$Al$_5$ IMC layer is largely regarded as the most brittle (11.8 ± 1.8 GPa) IMC phase in comparison to the other IMC phases, i.e., FeAl$_3$, Fe$_4$Al$_{13}$ and is the main reason for loss in mechanical properties of the weld. In addition, Cui et al. [11] found a negative correlation between the thickness of the IMC layer and ultimate tensile strength of the joint. Through electron backscatter diffraction (EBSD) mapping of failed specimens, they concluded intergranular fracture occurred along the Fe$_2$Al$_5$ IMC. They also found that the thickness of Fe$_2$Al$_5$ IMC layer could be reduced by increasing the cooling rate. Seffer et al. [12] compared the differences between aluminium-to-steel and steel-to-aluminium overlap configurations during laser welding. They found that when welding with aluminium on top, aluminium is necessarily overheated in order to transmit sufficient heat to the bottom to melt the steel. This is a consequence of the fact that aluminium is more reflective and has a lower melting temperature compared to steel. Therefore, aluminium-to-steel led to high amounts of mixing (between Fe and Al), excessive and more brittle Al-rich IMCs (FeAl$_2$, Fe$_2$Al$_5$, FeAl$_3$), cracking, and ultimately a loss in weld strength. The work in [13] concluded that the IMC layer was directly proportional to the peak temperature and a higher energy input led to the formation of more Al-rich IMCs, which were found to be more brittle than the Fe-rich IMCs (Fe$_3$Al, FeAl).

Some level of success to achieve structural joints between steel and aluminium has been obtained by solid-state joining processes, such as friction stir welding. Since with the solid-state joining the temperature in the process is below the melting point of the metals being joined, the risk of forming brittle IMCs is minimal [14]. Nonetheless, friction stir welding is limited to specific joint geometries - typically, only butt or overlapped joints. A number of fusion joining processes [4] have been proposed for joining steel to aluminium - they include arc welding, resistance spot welding, CMT welding, electron beam welding and laser beam welding (LBW). One of the attractive options has been LBW which has recently gained popularity due to progress in technology, making it comparatively affordable. The main advantage of LBW, due to its high energy density, is its ability to produce welds with minimal heat affected zone and high cooling rates. Coupled with ease of automation and no requirement for physical contact with the parts when using remote optics, LBW is nowadays adopted across various industries in a range of applications [15]. Recent advancements have allowed the introduction of sophisticated welding patterns enabled by beam oscillation and wobbling [16,17], fast beam repositioning with superior processing speeds (up to 100 mm/s for 2.5 mm aluminium plates) and power modulations in the range of few kHz. Among the technological advancements, laser beam shaping is now gaining popularity since it holds the promise to control cooling rates and thermal gradients in and around the molten pool. This theoretically leads to a tailored material response to the heat input both spatially and temporally. A tailored power density profile is generated via adequate insertion of optical components (specially coated lenses of silica substrate) in the optical chain of the welding head; or by electro-optical switching multiple laser beams generated in the laser source itself, and enabled by beam combiners with optical phased array [18]. Research has confirmed a positive effect of the laser beam shaping on the control of the weld profile and keyhole stabilization with suppressions of spatters and significant reduction of porosity in the weldments [19,20,21]. With the aim to control the micro-structure of the weld and limit the formation of centre-line cracks, Pamarthi et al. [22] applied the adjustable ring-mode (ARM) laser to remote laser welding (RLW) of 6005 aluminium alloys and results showed that the selection of the optimal power ratio (core/ring) promotes the wider formation of equiaxed grains and better grain refinement. These effects in turn can ensure stable material processing with improved weld quality [23] and smoother weld surface finishes due to a delayed solidification rate [24]. Wang et al. [20] found that the ARM laser had a much greater depth of penetration in core-only mode; whereas the ring beam in isolation mainly affected the average width of the fusion zone. The ring beam distributes the heat input across a wider spot compared to the core beam, and therefore lower weld penetration was achieved. This was mitigated by selecting an appropriate ratio between the diameters of the core and ring beams [25].

Although some potential benefits such as less spatter [25,33] and improved keyhole stability [20], better seam quality [34] and increased productivity [35] quoted for laser beam shaping, a clear understanding of intermetallic formation and microstructure morphology are not clearly reported. Table 1 shows some of the recent key applications of laser beam shaping. Yan et al. [30] found a reduction in IMC thickness, due to the use of a continuous (CW) and pulsed (PW) dual superimposed laser setup. They found a root-like weld pool structure (due to the PW beam) with a 10 μm IMC thickness, whereas a 94 μm IMC thickness was found with a single (core) beam setup. Mohammadpour et al. [7] and Xia et al. [31] also observed a reduced IMC thickness. Although both studies incorporated a dual and co-axial laser setup, they used a welding-brazing approach with AlSi12 filler material. Therefore, it is difficult to individually determine the exact reduction in IMC thickness due to the beam shaping technique alone.

This paper aims to study the impact of the adjustable ring-mode on the IMC formation, microstructure and mechanical properties during steel to aluminium laser welded lap joints. This will be achieved by considering three welding modes (conduction mode, keyhole mode in partial and full penetration) and the three selected laser beam shapes (core-dominant beam; ring-dominant beam; intermediate-core beam). The relevance of studying both conduction and keyhole mode is explained by the fact that conduction mode welding allows minimising metal mixing with low to neglectable turbulence in the molten pool and hence controlling the IMC layer; conduction mode is typically achieved by laser beam defocussing to enlarge the laser spot diameter – this is regarded as a cheap and easy-to-integrate solution to enable beam shaping. Nonetheless, conduction mode is limited by the material thickness which can be processed. Keyhole mode welding, instead, helps to overcome this issue since it allows to reach deep weld penetrations at high aspect ratios; however, higher heat inputs compared to conduction mode are required, and this typically leads to higher IMC formation. Therefore, in order to highlight the distinctive properties of the adjustable ring-mode laser, this paper will study both welding modes. The discussion of the results will be presented by linking key process parameters (total laser power, power ratio and power density) to the chemical, microstructural and mechanical data of remote laser welded IF

Table 1
Key applications of laser beam shaping for processing similar and dissimilar materials.

Material(s)	Laser beam shaping technique		Key finding(s)	Ref.
Silicon	Ring shape	Ring shaped beam	Larger lateral heat distribution at a lower peak temperature.	[26]
Stainless and mild steel		Dual & co-axial beams (ARM laser)	Adequate weld penetration, keyhole stability, and reduces the spatters.	[20,25]
AA6082	Multiple spots	Multi-focus axial beam shaping	Homogenous heat distribution, keyhole stabilisation and reduces the spatters.	[27]
Stainless and mild steel		Beam splitting, parallel 3 to 7 beams	Improve melting efficiency, leading to less total power required.	[28]
DP590 steel to AA7075		Twin laser spots (0.8 mm apart)	Allowed a tailored heat distribution between metals, as well as spot shape and size.	[29]
JSC270CC steel to AA6111-T4	Dual and co-axial	Dual superimposed beams; continuous and pulsed	Reduce/avoid blowholes and reduce IMC layer to 10 μm.	[30]
Low carbon steel to AA6022		Dual overlapping beams, horizontal or vertical variations	Reduced IMC layer to 10 μm.	[7]
DP590 steel to AA6061			Horizontal laser setup allowed for a reduced and homogenous IMC layer due to lower peak temperature and smaller temperature gradient.	[31]
AA5052	An "infinite-shaped (∞)" beam		Improve weld surface quality, reduced spatters, better toughness and UTS, finer grain size.	[32]

steel [6] to 1050 aluminium [36,37]. The choice of both alloys was based on the lean composition, without the presence of major alloying elements. In doing so, this study will point-out the primary effects of the adjustable ring-mode laser and isolate the role of the processing parameters, rather than the effects of complex metallurgical characteristics which may occur with high alloyed materials.

2. Experimental procedures

2.1. Materials

The LBW process was performed between an interstitial free (IF) steel and a 1050 aluminium alloy, which were 1 and 3 mm in thickness, respectively. Both materials were un-coated and industrially supplied sheets were sectioned into rectangular coupons of 38 mm in width and 120 mm in length using a guillotine cutter, the coupons were then chemically cleaned with acetone to remove any surface contaminations before welding. Chemical compositions measured by optical emission spectroscopy (OES) for both materials are given in Table 2.

2.2. Laser beam shaping system

A Coherent fibre laser (Coherent ARM FL10000) with a maximum combined power of 10 kW with an adjustable ring-mode was used for the LBW trials. The ARM laser beam was delivered through a WeldMaster Scan&Track remote welding head (YW52 Precitec GmbH), which was mounted on a 6-axis robot system from ABB robotics (Table 3). No filler wire or shielding gas was used for any of the trials and all trials were conducted at a 3° beam incidence angle with no beam oscillation and no part-to-part gap.

The focal offset (A_z) was taken as the distance between the focal point of the laser beam and the welding surface (i.e., it is 0 mm when the focal point is on the top (steel) surface). The optical fibre for the core and ring beams were 100 and 290 μm in diameter, respectively; each beam provided a maximum power of 5000 W. The power ratio, r, is defined as the core power, P_C, divided by

Table 3
Details of the laser beam shaping system.

Parameters	Units	Core	Ring
Maximum power	W	5000	5000
Optical fiber diameter	μm	100	290
Spot diameter on focus	mm	0.20	0.58
Collimating length	mm	150	
Focusing length	mm	300	
Wavelength	nm	1070 ± 10	

the ring power, P_R. At r = 0 a ring-only beam is produced, whereas at r = ∞, a core-only beam is produced. Schematic representation of some representative power distributions of the ARM laser at various power ratios are shown in Fig. 1.

2.3. Design of experiments

Table 4 shows the selected combinations of P_C, P_R and r, in conjunction with the related power density, P_d, and ultimate tensile strength, UTS. The P_d is defined in **Equation (1)**, where A_s is the area of the laser spot for the given beam shape profile and measured at the metal surface; $P_T = P_C + P_R$ is the total power applied through the laser spot. The area of the core and ring beams were extracted from the PRIMES GmbH laser power measurement system.

$$P_d = \frac{P_T}{A_s} \left[\frac{MW}{cm^2}\right] \tag{1}$$

A schematic representation of the welding setup is shown in Fig. 2. All trials were performed at a welding speed of 4 m/min and focal offset (A_z) of 16 mm. The selected focal offset allowed to achieve approximately 1.25 mm and 1.65 mm spot diameters at the core and ring beams, respectively. The trials were grouped into 3 sets, based on their core/ring power ratios, namely: maximum core (MC), maximum ring (MR) and intermediate core (IC).

Table 2
Chemical compositions of the interstitial free (IF) steel and 1050 aluminium alloy, measured by OES (in wt%).

IF steel	Fe	C	Mn	Al	Si	S	Ultimate Tensile Strength (N/mm²)
	balance	0.05	0.165	0.05	0.03	0.01	210

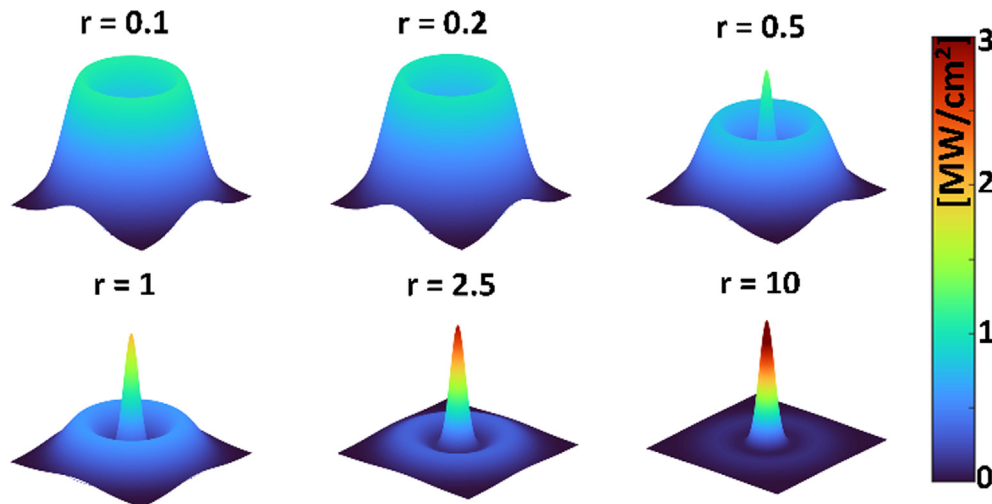| Aluminium Alloy (1050)	Al	Si	Fe	Cu	Mg	Ti	Ultimate Tensile Strength (N/mm²)
	balance	0.08	0.47	0.006	0.001	0.025	110

Fig. 1. Schematic representations of the power ratios, r, between core and ring beam.

Table 4
List of conducted LBW experiments.

Trial set	Trial ID	Power [W]			Power Ratio, $r = P_C/P_R$ [–]	Power density, P_d [MW/cm²]	UTS [N/mm²]
		Core, P_C [W]	Ring, P_R [W]	Total, P_T [W]			
MC (No ring and variable core)	1	3000	0	3000	∞	0.25	68.2
	2	3500	0	3500	∞	0.29	52.1
	3	4000	0	4000	∞	0.33	31.7
	4	4500	0	4500	∞	0.38	22.6
	5	5000	0	5000	∞	0.42	39.3
MC (Max core and variable ring)	6	5000	500	5500	10	0.26	54.5
	7	5000	1000	6000	5	0.29	35.6
	8	5000	1500	6500	3.33	0.31	27.0
	9	5000	2000	7000	2.5	0.33	19.7
	10	5000	2500	7500	2	0.36	17.6
MR (Max ring and variable core)	11	500	5000	5500	0.1	0.26	74.1
	12	1000	5000	6000	0.2	0.29	97.6
	13	1500	5000	6500	0.3	0.31	58.8
	14	2000	5000	7000	0.4	0.33	25.8
	15	2500	5000	7500	0.5	0.36	28.3
IC (Intermediate core and variable ring)	16	1500	3000	4500	0.5	0.21	82.4
	17	1500	3500	5000	0.43	0.24	84.7
	18	3000	1500	4500	2	0.21	54.4
	19	3000	2000	5000	1.5	0.24	33.5
	20	3000	2500	5500	1.2	0.26	35.3
	21	3000	3000	6000	1	0.29	43.7
	22	3000	3500	6500	0.86	0.31	39.7

(1) *Maximum core (MC)* – this case includes two subsets: the first one used no ring power and the core increases from 3000 to 5000 in 500 W increments; the second sub-set utilised maximum 5000 W core power with variation in the ring power from 0 to 2500 W in 500 W increments;

(2) *Maximum ring (MR)* – maximum 5000 W ring power with variation in the core in 500 W increments; and,

(3) *Intermediate core (IC)* – variation in the ring power from 1500 to 3500 W in 500 W increments and 2 fixed core power levels at 1500 W (sufficient to achieve conduction mode) and 3000 W to achieve keyhole mode (partial and full penetration).

2.4. Characterisation techniques

The laser welded samples were prepared using the following metallographic procedure: first, samples were sectioned into 3 weld cross-sections per trial, one in the middle and two at 10 mm away from the weld end/start to ensure a steady state of the laser weld. Samples were mounted in a conductive bakelite resin and polished down to 0.02 μm, via steps of coarse and fine grinding, and 9 μm and 3 μm polishing.

A Keyence VHX7000 light microscope was used to acquire macro-scale optical images, which were used to take quantitative measurements on key characteristics (using image analysis software ImageJ) and qualitative observations. The aspect ratio of the weld was defined as ratio between weld depth and width (Fig. 2**b**). For aspect ratios ≤ 1.0 the weld is defined as conduction mode, and any aspect ratio above 1.0 is associated to keyhole mode with either partial or full penetration to the bottom (Al) sheet. Correlation among weld characteristics were assessed using Pearson's correlation coefficient: values of correlation close to 100% (or -100%) indicates perfect positive (or negative) correlation, whereas values close to zero shows no meaningful relationship between variables.
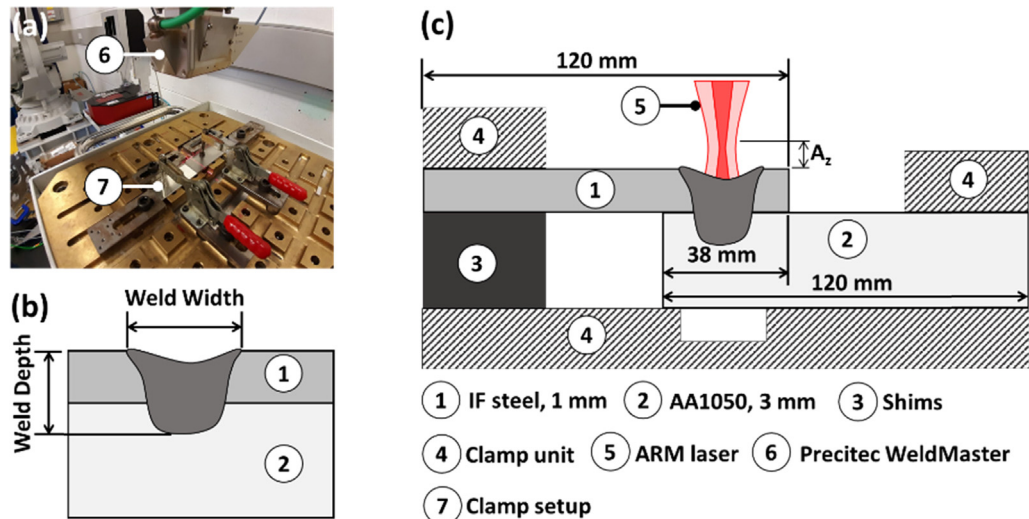
Fig. 2. (a) welding setup; (b) definition of the weld profile (depth and width); (c) schematic showing the specimens and the clamp setup (not to scale).

An FEI Versa 3D dual-beam scanning electron microscope (SEM) equipped with energy dispersive x-ray spectroscopy (EDS) and electron back-scatter diffraction (EBSD) was used for microstructural analysis. EDS was used for low magnification montage chemical mapping of welds for studies on the mixing of Fe and Al, an accelerating voltage of 20 kV was used with a current of 16 nA, providing input counts of up to 300,000 cps, with a dwell time of 250 ms. EBSD was used for automatic grain size measurements using Oxford Instruments software: AZtec Crystal in the top sheet of the welded sections for selected full penetration keyhole trials. An accelerating voltage of 20 kV and a current of 25 nA were used for EBSD the mapping. Working distances were kept at 20 mm and a step size of 0.3 μm was used. SEM backscattered electron images (SEM-BSE) were used to take measurements for IMC thicknesses − 15 measurements were taken for each instance which provided the average and standard deviation.

2.5. Mechanical testing

The lap-shear mechanical testing was performed on the laser welded coupons using an Instron 30 kN tensile testing machine, in accordance with the BS EN ISO 14273 standard [38]. For each weld ID, one replication per test was performed. A Wilson Vickers micro-hardness tester was used for performing indentation maps across the laser welded cross-sections which were metallographically prepared. A load of 0.2 kgf was used with a spacing of 0.3 mm between indents.

2.6. Thermo-Calc simulations

Thermodynamic simulations were performed using Thermo-Calc, at equilibrium conditions using the steels and Fe-alloys package with the TCFE-10 database. Thermo-Calc uses CALPHAD based experimental approaches for simulations. The compositions for Fe and Al used in the simulations were provided via SEM-EDS mapping and were used to predict the amount in volume % (vol%) of the IMC phases in the weld pools of interest.

3. Experimental results

3.1. Overview of the weld microstructures

The cross-sections are shown in Fig. 3 and discussed as follows:

- *MC trials* - With only core power, the welds are initially in a shallow conduction mode (ID 1 and 2) and then transition into partial penetration keyhole mode (ID 3–5), which shows significant cracking. As the ring power is increased from 0 to 1000 W, full penetration keyhole mode welding appears at ID 7 which shows no significant cracking with little Fe-rich depth. As the ring power is increased to 2000 and 2500 W (ID 9 and 10) the depth of the Fe-rich region increases. At 2500 W ring power (ID 10) excessive cracking is observed.

- *MR trials* - At core power between 500 and 1000 W (ID 11 and 12) the weld is in conduction mode; comparing ID 12 to ID 7 it is worth noting that although the total power (6000 W) is the same, ID 7 achieves a keyhole mode. This is a consequence of the fact that the power density significantly drops at ID 12 due to the ring-dominant behaviour (r = 0.2). Full penetration keyhole mode is achieved when the total power reaches 7500 W (ID 15), which is significantly higher than the 6000 W used in ID 7 for the same full penetration.

- *IC trials* - With a core power of 1500 W, conduction mode was achieved with ring power of 3000 W and 3500 W (ID 16 and 17). With a fixed core power of 3000 W and ring power between 1500 W and 2500 W (ID 19 and 20), partial penetration keyhole mode was achieved with significant cracking observed at the interface of Fe- and Al-rich interfaces. When the ring power is at 3000 and 3500 W (ID 21 and 22), full penetration keyhole mode is achieved.

3.2. Lap-shear testing results

Lap-shear mechanical testing was used to measure the UTS of each weld as well as the extension at the UTS. Fig. 4 shows the relationship between the UTS and the power ratios with reference to the total power used. At r = ∞ (core-only beam) a significant variation in the UTS is observed against the total power used (Fig. 4a): the highest strength (68.2 N/mm²) was achieved at the lowest total power (3000 W). Nonetheless, the absolute greatest UTS was achieved with the ID 12/ MR trial with a power ratio of 0.2 and UTS of 97.6 N/mm², which was closely followed by the IC trials, ID 16 and 17, corresponding to 4500 and 5000 W, respectively. For power ratios between 2 and 10 (ID 6 to 10), results show that the greater the power ratio the higher the UTS, with a strong linear correlation (approximately 99%). This is confirmed in Fig. 3 which shows excessive cracking especially in ID 9 and 10; but also in
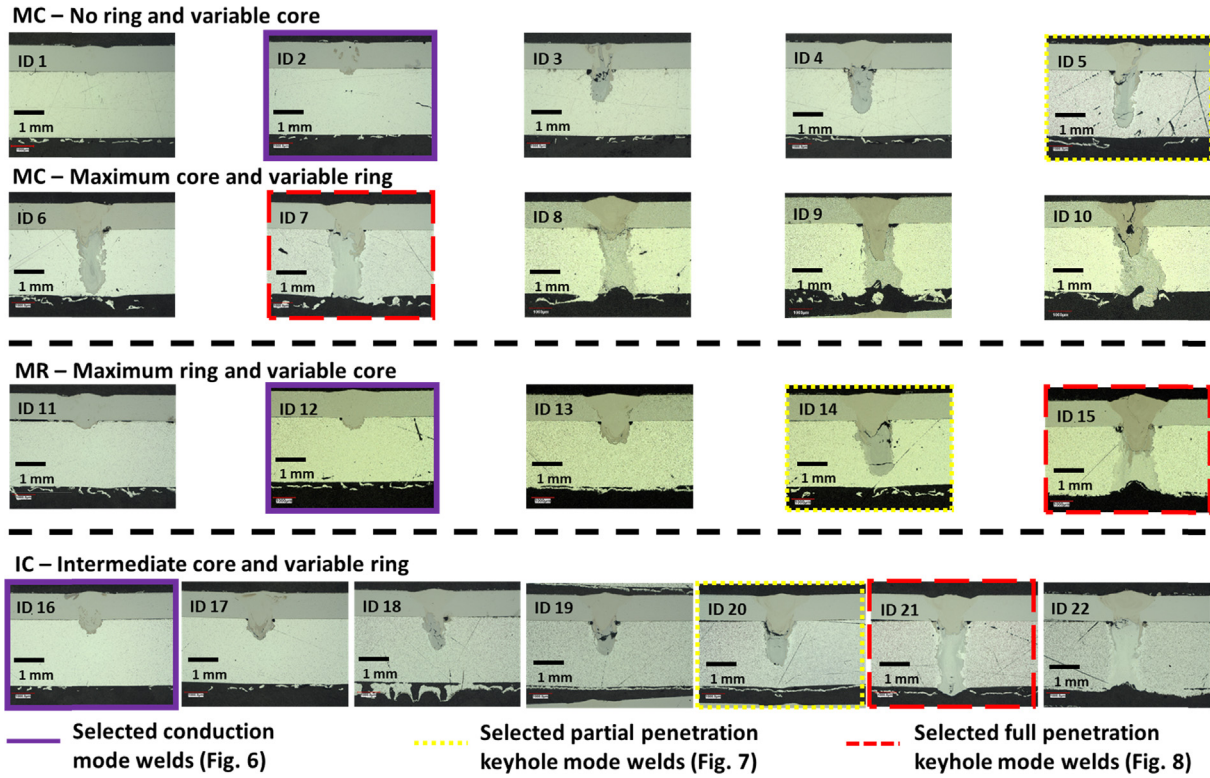
Fig. 3. Optical micrographs showing representative cross-sections for each of the weld IDs. Highlighted weld IDs are discussed in more details in Figs. 6-8.
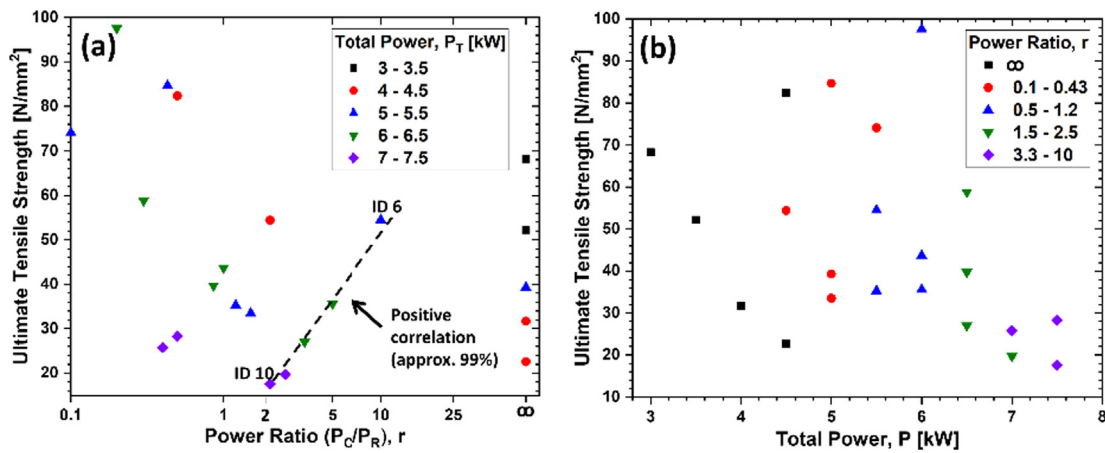
Fig. 4. Graphs showing (a) the ultimate tensile strength (UTS) versus the power ratios and (b) total power for all the welding trials.

Fig. 4**b** which categorises the UTS data with the total power shown on the x-axis - individual trends are identified from each power ratio grouping (i.e., r = ∞, 0.1–0.43, 0.5–1.2), and a negative correlation between the UTS and total power can be observed, so as the total power increases within the power ratio groups, the UTS decreases.

3.3. Effect of weld pool geometries on lap-shear strengths

The relationships between the UTS and the aspect ratios and penetration depths are observed in Fig. 5**a** and **b**, respectively. The UTS versus aspect ratio (Fig. 5**a**) shows a negative correlation of 73%, in which conduction mode trials with the lower aspect ratios (0.6 – 1.0) achieved the greatest strengths $\geq$ 65 N/mm^2 – the penetration depths for these trials were in the range 1.2 –

2.0 mm (Fig. 5**b**). It is difficult to correlate the effects of the power density on the penetration depth of the welds (Fig. 5**d**) - this is because when the ring beam is used, P_d is increased however less penetrative effect is supplied in comparison to the higher power density core beam [20]. When using only a single core beam, the work in [6] found that P_d is correlated with the penetration depths of the welds.

The individual sets of trials also showed distinct trends:

- *MC trials* - a very similar aspect ratio was measured for all the trials which were in full penetration keyhole mode. However, the UTS for these trials showed a significant spread (15 – 55 N/mm^2) which was due to the variation in P_d between 0.29 and 0.36 MW/cm^2 (ID 7 – 10). The trials with the greater P_d showed significant cracking, and therefore failed prematurely
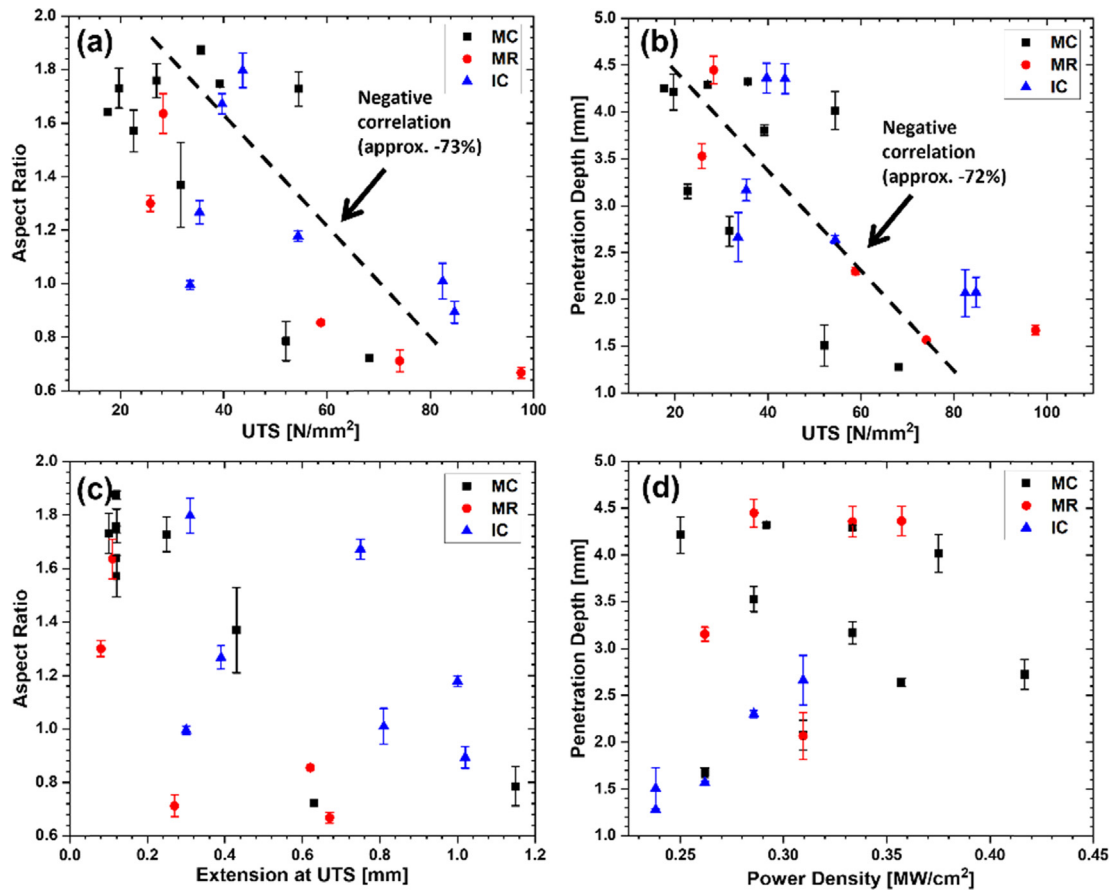
Fig. 5. Graphs showing (a) the aspect ratio versus the UTS, (c) extension and (b) the penetration depth versus the UTS and (d) the power density for all the welding trials.

during the lap-shear tests. The two conduction mode trials (ID 1 and 2) showed significantly lower aspect ratios and greater strengths.

- *MR trials* - there are 2 groups in Fig. 5a, the first group with high aspect ratios and low strength (approximately 26 N/mm^2) and characterised by keyhole welds (partial and full penetration); the second group shows lower aspect ratios (approximate from 0.6 – 1) and high strengths (approximately higher than 60 N/mm^2) and characterised by conduction mode.
- *IC trials* - they showed an intermediate response between the MC and MR trials.

The aspect ratio versus extension data (Fig. 5c) shows a large spread, although when analysing each individual trial set, a general trend is identified for each instance. For the MC trials it was found that: the group with the high aspect ratio and small extension (below 0.2 mm) are the keyhole (partial and full penetration) welds, which are very brittle due to high amounts of metal mixing, subsequent IMC formation and cracking. The second group are the conduction mode welds at lower aspect ratio; these have notably greater extension (above 0.8 mm). The MR and IC trial sets also show a very similar trend but are not as distinctly grouped together like the MC trials. The data presented in Fig. 5c shows that the conduction mode welds presented the greatest ductility, as compared to the other welding modes (keyhole, both partial and full penetration) with lower aspect ratios. The greater IMC formation in the Al-rich side of the weld pools in the keyhole mode (partial and full penetration) welds lead to brittleness of the welded joint as also noted by Seffer et al. [12].

3.4. Effect on the chemical compositions and micro-hardness

The mixing of the Fe and Al determines the weld pool composition and has a significant effect on the formation of IMCs. The IMCs influence the micro-hardness of the welded joint. Due to the differences in micro-hardness (brittleness) relative to the base materials, cracks are known to initiate and propagate from these IMC phases. Local compositions in the welds were measured in the top and bottom regions (red asterisk in Figs. 6-8). These compositions were used to identify the IMC phases which had formed in the bottom of the weld pool using the Fe-Al binary phase diagram [39]. Locally measured compositions, average micro-hardness values, predicted IMC phases and weld strengths are summarised in Table 5 for the three welding modes (conduction mode, keyhole mode in partial and full penetration) and the three selected laser beam shapes (core-dominant beam, MC; ring-dominant beam, MR; intermediate-core beam, IC).

Key findings are presented as follows:

- *Conduction mode welding* (Fig. 6) - When comparing the conduction mode trials, a thin IMC layer was observed in the Fe-Al interface; due to the continuous layer, it was comparable across the three welds. A schematic diagram showing how the IMC layers were measured is shown in Fig. 6g. Measurements were taken evenly along the complete cross-section of the weld interface. For total IMC thickness, measurements were taken from the start of the IMC layer (at the steel interface) to the end of the IMC layer (at the Al interface). The Fe$_2$Al$_5$ layer was accurately measured due to the visual differences (shade and mor-
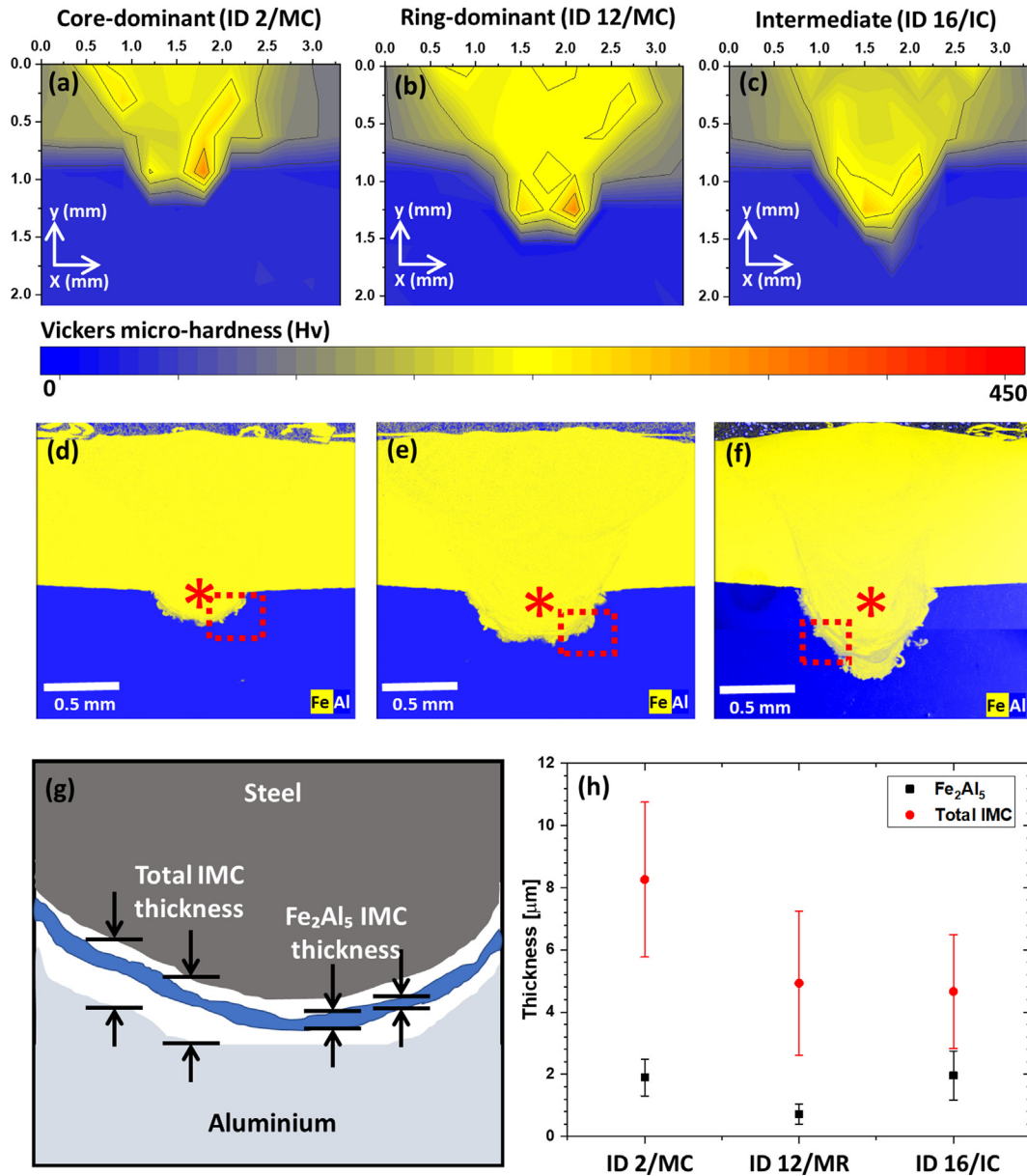
Fig. 6. Vickers micro-hardness indentation contour maps (a-c) and corresponding SEM-EDS chemical maps (d-f) for the representative conduction mode welds. Red asterisks signify regions where EDS compositions were extracted for Table 5 and the red dotted boxes signify where EDS maps were performed for Fig. 10. Schematic representation (g) of the steel to aluminium interface; (h) Fe_2Al_5 and total IMC thicknesses for the conduction mode welds.

phology) as well as composition difference measured through SEM-EDS. The MC trial had the thickest total IMC layer at 8.26 μm (Fig. 6h), whereas the MR and IC trials had considerably thinner total IMC layers, average of 4.9 μm and 4.6 μm, respectively. When comparing the individual Fe_2Al_5 IMC layer, the MR trial showed the thinnest, which was approximately 0.7 μm, whereas the MC and IC trials both measured approximate 2 μm on average.

- *Partial penetration keyhole mode welding* (Fig. 7) - In the bottom of the weld pool, for the MR and IC trials the Fe_4Al_{13} and/or $FeAl_3$ IMC phase were found based on the EDS composition and binary phase diagram [39]; for the MC trial the Fe_4Al_{13} IMC was predicted due to a greater Al content (66.9 wt%). When comparing this data with Thermo-Calc vol% predictions, the simulation predicted the MC trial to contain the least amount of Fe_4Al_{13} (81%) and the MR and IC trials to contain a greater amount (95 and 100%, respectively). When comparing these

values with the average micro-hardness achieved in the bottom of the weld pool region a trend is identified: the MC trial which has the least predicted Fe_4Al_{13} had a micro-hardness of 350 Hv, whereas the MR and IC trials with greater amounts of Fe_4Al_{13} possessed micro-hardness of 600 and 550 Hv, respectively.

- *Full penetration keyhole mode welding* (Fig. 8) - The EDS compositions in the full penetration keyhole trials showed distinct variations in both the top and bottom of the welds. With regards to the IMC formation in the bottom of the full penetration keyhole welds, all 3 welds contained the Fe_4Al_{13} IMC according to the Fe-Al binary phase diagram [39]. Although the MR trial contained a greater amount of Al (84.6 wt%) compared to the MC and IC trials (72.4 and 71.5 wt%, respectively), the Thermo-Calc vol% predictions suggested that the MR trial contained the least amount of Fe_4Al_{13} (32%) and both the MC and IC trials contained similar amounts (64 and 67 %, respectively). The Thermo-Calc predictions also correlated with the
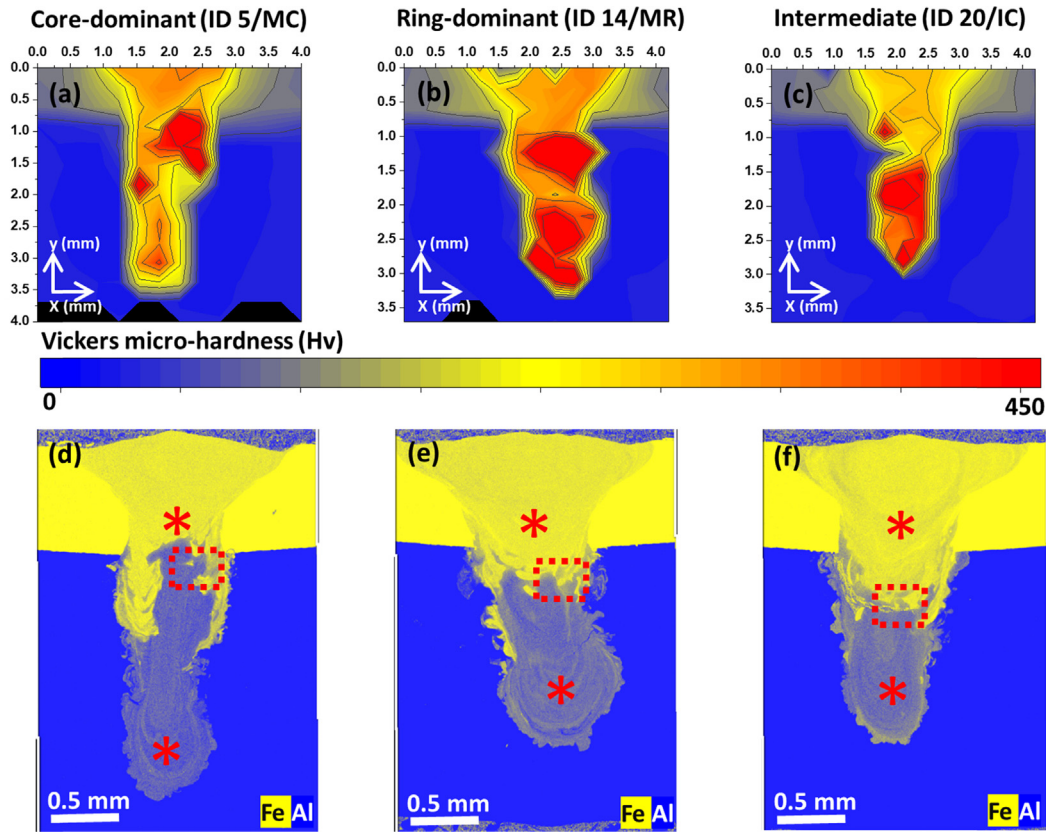
Fig. 7. Vickers micro-hardness indentation contour maps (a-c) and corresponding SEM-EDS chemical maps (d-f) for the representative partial penetration keyhole mode welds. Red asterisks signify regions where EDS compositions were extracted for Table 5 and the red dotted boxes signify where EDS maps were performed for Fig. 10.

micro-hardness averages acquired in the bottom of the weld pools. For the MR trial with the least amount of Fe_4Al_{13} an average of 100 Hv was acquired, and 175 Hv and 200 Hv were obtained for the MC and IC trials. For the MR trial up to 23 wt % of Al was measured in the top of the weld pool, compared to the MC and IC trials which only contained 13.3 and 12.1 wt %, respectively. The effect of the difference in Al content in the top of the weld pools is analysed in Fig. 9 through the grain structure acquired by EBSD mapping. For the MC and IC trials a coarse grain structure is observed in the centre of the welds, whereas for the MR trial a very fine equiaxed grain structure is observed in the same region. These differences can be due to the amount of Al solute which has mixed into the steel upper section leading to grain refinement: the MR trial, with the size range below 100 μm, contains notably more grains due to the fine equiaxed solidified structure.

4. Discussion

The impact of laser beam shaping, in the form of adjustable ring-mode, is discussed considering the three welding modes (conduction mode, keyhole mode in partial and full penetration) and the three selected laser beam shapes (core-dominant beam, MC; ring-dominant beam, MR; intermediate-core beam, IC). The discussion is presented by linking the main process parameters (total laser power, P_T, power ratio, r, and power density, P_d) to the chemical, microstructural and mechanical data. The representative weld trials with key results are summarised in Table 5.

Conduction mode welding - With regards to the conduction mode (Fig. 6), ring-dominant beam (ID 12/ MR) tends to create a wider weld pool compared to the core-only beam (ID 2/ MC). This

is consequence of the fact that the ring spot is larger (1.65 mm) than the core spot (1.25 mm). The same results were obtained by Duocastella and Arnold [26] who demonstrated that the rate of heat transfer is greater with the ring-dominant beam as compared to the conventional core-only beam. It is however worth noting that, while the power density values of ID 2/ MC and 12 are same and equal to 0.29 MW/cm^2, the ID 2/ MC is a core-only beam with the full power of 3000 W, and ID 12/ MR has total power of 6000 W applied across the ring spot, of which 1000 W across the core spot. Pre-screening welding trials confirmed that no penetration in the bottom sheet would be obtained if, at the same power density, the full power (5000 W) of ID 12/ MR would be delivered only through the ring beam. This helps to corroborate the fact that the optimal selection of the total power, corresponding power density and power ratio is critical to control the weld properties. It is observed that the core beam facilitates the opening and deepening of the molten pool and the ring beam helps to widen the molten pool. This has direct implication to the strength of the joints: ID 12/ MR performed the best with 97.6 N/mm^2 (joint efficiency 71%) followed by the ID 16/ IC at 82.4 N/mm^2, and the ID 2/ MC at 52.1 N/mm^2. The variation in strength is however not directly correlated to the micro-hardness, which shows neglectable variations (average value of 215 Hv at the Fe interface) across the 3 trials. This is explained by the fact that the welds ID 2, 12 and 16 were in conduction mode, therefore the mixing between the Fe and Al was minimal, and predominantly in the weld pool interfaces. This also suggests that higher strength is achieved by simultaneously reducing the mixing of the dissimilar materials and increasing the weld width. This was confirmed by Jarwitz et al. [16] who used laser beam oscillation to enlarge the molten pool in order to improve the mechanical strength.
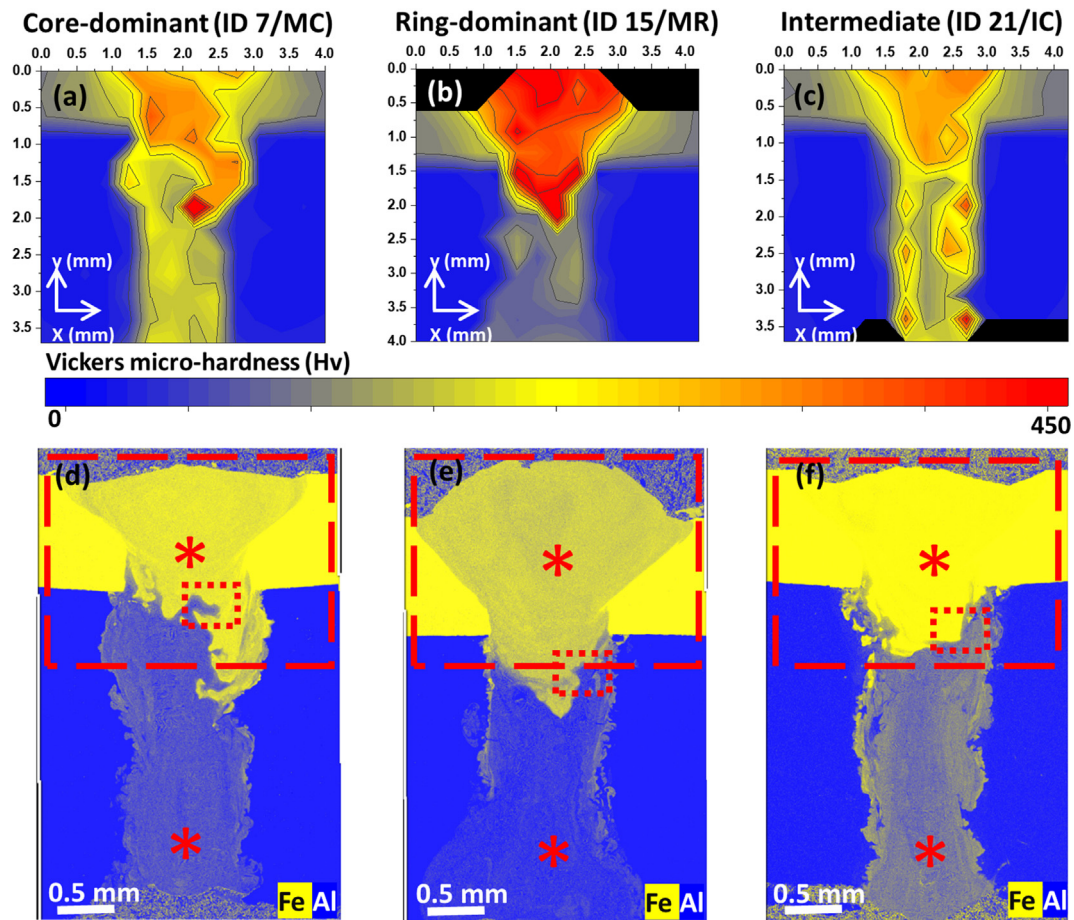
Fig. 8. Vickers micro-hardness indentation contour maps (a-c) and corresponding SEM-EDS chemical maps (d-f) for the representative full penetration keyhole mode welds. Red asterisks signify regions where EDS compositions were extracted for Table 5 and the red dotted boxes signify where EDS maps were performed for Fig. 10.

Table 5
Summary of key chemical, microstructural and mechanical data, including EDS-mapping derived compositions of the Al and Fe from the top and bottom of the welds shown in Figs. 6-8, average Vickers micro-hardness, possible phases, and lap-shear strengths.

Trial set and ID	P_T (kW)/ Power ratio, r	P_d (MW/ cm²)	Al: Fe Compositions (wt %)		Average Vickers Micro-hardness	IMC thicknesses in conduction mode welds (µm)	Possible IMC Phase(s) (Bottom of Weld Pool)		Lap-shear Strength (N/ mm²)	Joint Efficiency (%)
			Top	Bottom	Top: Bottom	Fe_2Al_5: Total IMC	Phase Diagram Predictions	Thermo-Calc Predictions (All Fe_4Al_{13} vol%)		
Conduction Mode										
MC 2	3500/∞	0.29	4.4: 95.6	75.1:24.9	215: –	1.90: 8.27	–	–	52.1	38
MR 12	6000/0.2	0.29	5.1: 94.9	78.3:21.7	215: –	0.71: 4.93		–	97.6	71
IC 16	4500/0.5	0.21	3.5: 96.5	73.9: 26.1	215: –	1.96: 4.70		–	82.4	60
Partial Penetration Keyhole Mode										
MC 5	5000/∞	0.42	12.9: 87.1	66.9: 33.1	320: 350	–	Fe_4Al_{13}	81	39.3	29
MR 14	7000/.4	0.33	13.8: 86.2	62.6: 37.4	320: 600	–	Fe_4Al_{13} and/or $FeAl_3$	95	25.8	19
IC 20	5500/1.2	0.26	12.7: 87.3	61.2: 38.8	285: 550	–		100	35.3	26
Full Penetration Keyhole Mode										
MC 7	6000/5	0.29	13.3: 86.7	72.4: 27.6	300: 175	–	Fe_4Al_{13}	64	43.7	32
MR 15	7000/0.5	0.36	23.0: 77.0	84.6: 15.4	400: 100	–	Fe_4Al_{13}	32	28.3	21
IC 21	6000/1	0.29	12.1: 87.9	71.5: 28.5	300: 200	–	Fe_4Al_{13}	67	35.6	26

(a) core-dominant - ID 7/MC

(b) ring-dominant - ID 15/MR

(c) intermediate - ID 21/IC
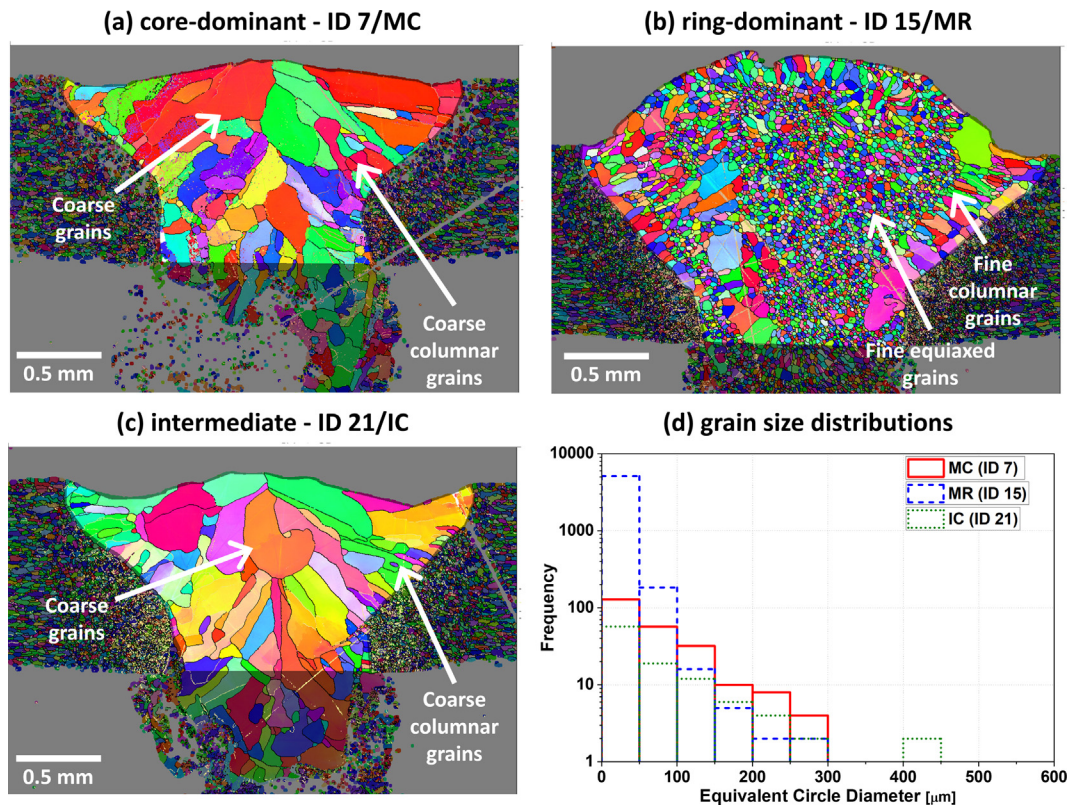
(d) grain size distributions

Fig. 9. EBSD maps showing the grain sizes in the Fe-rich regions (top sheet) for the full penetration keyhole mode trials with quantification of the grain size distributions.

When comparing the depth of the three conduction mode trials, although ID 2/ MC was the shallowest (1.48 mm), it has the thickest total IMC layer (average 8.27 μm). The opposite was observed for ID 12/ MR with the deepest measured depth of 1.59 mm and the total IMC layer of 4.93 μm. Although ID 12/ MR only had 500 W less power from the core beam than the ID 16/ IC, it contained a considerably thinner Fe_2Al_5 IMC layer. It is known that the formation and growth of Al–Fe IMCs is dependent on local temperature and change of the concentrations of solute atoms. Through numerical simulations, Mohammadpour et al. [7] found a temperature in the range of 700–900 °C was optimal for the growth of Fe_xAl_y interfacial IMCs. In a previous study, Sun et al. [40] modelled the thermal response of the adjustable ring-mode laser and they found that a higher power ratio (which corresponds to ID 2/ MC with r = ∞) results in higher peak temperatures prior to solidification. It was found [41] that higher peak temperatures generally tend to form thicker IMC layers. Therefore, it can be concluded that the growth of the total IMC and Fe_2Al_5 layers to be greater when the core-dominant beam setup is used. The Fe_2Al_5 IMC is found to be the most brittle and weakest in terms of bonding strength, which makes it susceptible to crack initiation [6,11].

At the interfaces of the 3 conduction mode welds (Fig. 10**a-c**) 3 IMC phases were observed: $FeAl_2$, Fe_2Al_5 and Fe_4Al_{13}. $FeAl_2$ and Fe_2Al_5 are located closer to the Fe-rich region whereas the Al-rich Fe_4Al_{13} is present in the form of needle-like structures in the Al side of the weld interface. Fine cracks tend to initiate in the Fe_2Al_5 region which is commonly reported in steel to aluminium laser welds [6,11,42]. The brittle Fe_2Al_5 is located in between other IMCs and the weld matrix, and the difference in thermal expansion coefficients during rapid cooling of the LBW process leads to solidification cracking [43]. Further to this, Meng et al. [17] suggested a higher melting of Fe (Steel), results in the a higher dissolution rate of Fe atoms in the liquid Al. In the current study this can be related

to a core-dominant beam setup, due to the greater power density of the core beam.

$$Fe(l) + Al(l) \rightarrow Fe_2Al_5(s) + Al(l) \rightarrow Fe_4Al_{13}(s) \qquad (2)$$
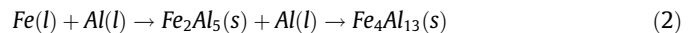
The Fe_2Al_5 IMC nucleates Eq. (2) preferentially before $FeAl_3$ (or Fe_4Al_{13} at non-equilibrium conditions) because of the higher solidification point (∼1173 °C versus ∼ 1160 °C, respectively). Due to excessive melting, if the Fe concentration is still sufficient at the weld interface, then the peritectic reaction would occur and a layer of Fe_4Al_{13} will also form.

Keyhole mode welding - Keyhole mode trials exhibit significant material mixing as observed in Figs. 7 and 8. Particularly, the MC trials present uneven distribution of Fe, while the ring-dominant beam in MR or the intermediate-core beam in IC creates more uniform distribution. The multi-physical simulations of the keyhole dynamics by Chianese et al. [44] suggested that the localised power density in MC trials determines upward flows that enhance mixing between parent metals and lead to formation of Fe-rich structures and clusters, whereas the use of a wider spot (MR and IC trials) tends to reduce material mixing and therefore leads to more uniform distribution of Fe in the molten pool.

The phase diagram predictions for the IMC formation in the bottom of the welds only suggests the possible IMCs which may form, however the Thermo-Calc predictions provided a quantitative estimate of the vol% of the IMC phase. The Fe_4Al_{13} IMC was predicted for all the welds with a fine needle-like morphology [6,11], as seen in Fig. 10**d-i**. For the keyhole mode (partial and full penetration) welds the Fe_4Al_{13} extended from the Fe-Al interface region to the bottom of each weld. In the bottom section of the weld pools, the Thermo-Calc simulations only predicted the Fe_4Al_{13}, however with varying quantities. No trend was found between the MC, MR or IC weld trials and the Fe_4Al_{13} content. The vol% of the Fe_4Al_{13} is well correlated (Pearson linear correlation: 92%) with the aver-
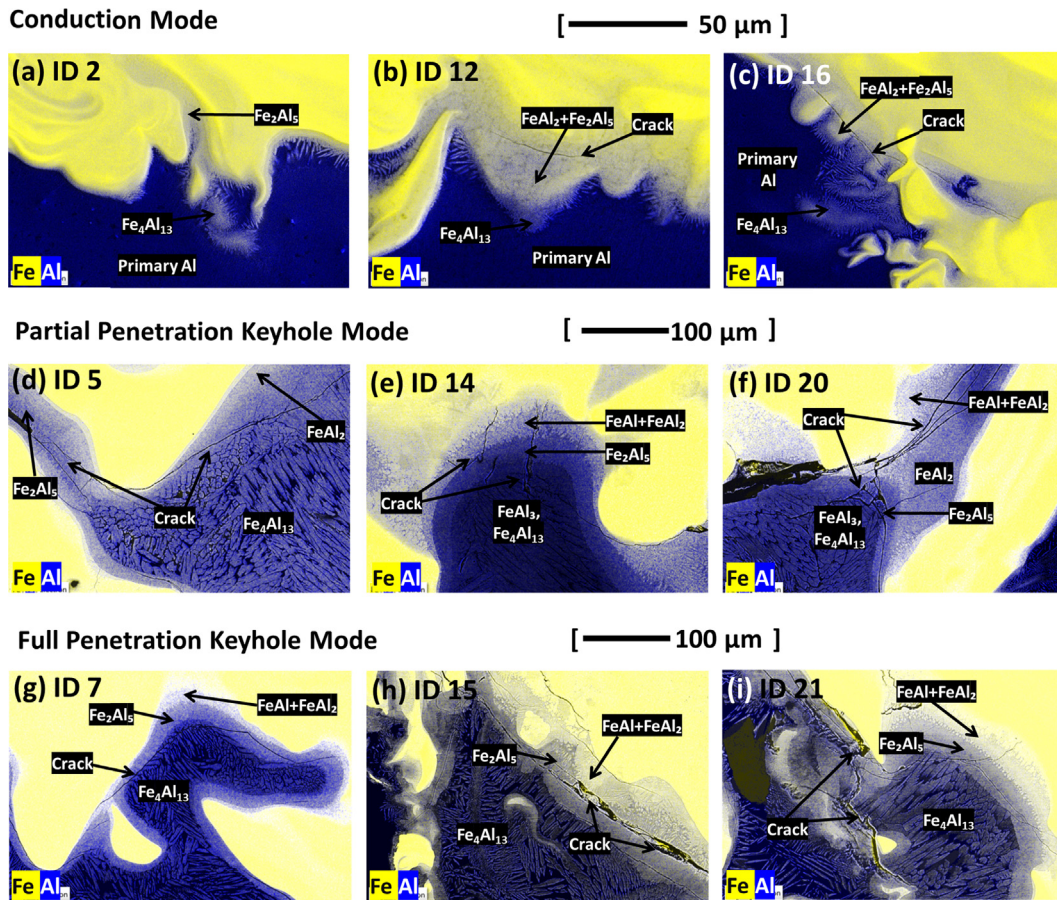
Fig. 10. SEM-EDS maps of the Fe-rich and Al-rich interfaces taken from the red dotted boxes in the conduction and keyhole mode (both partial and full penetration) welds shown in Figs. 6-8.

age micro-hardness values measured in the six welds for the keyhole mode (Table 5). In particular, for the partial penetration keyhole welds, 81, 95 and 100 vol% of Fe_4Al_{13} was predicted by Thermo-Calc for the MC, MR and IC trials in the bottom of the welds. The average micro-hardness measured in these same regions was 350, 600 and 550 Hv. Similarly for the full penetration keyhole mode welds, 64, 32 and 67 vol% of Fe_4Al_{13} was predicted by Thermo-Calc for the MC, MR and IC trials, respectively; and the average micro-hardness measured were 175, 100 and 200 Hv, respectively. The Fe_4Al_{13} IMC is known to possess a micro-hardness similar to that of $FeAl_3$ [6] due to the similar stoichiometric ratio (approximately 1:3 of Fe:Al), and it was found in [43] that $FeAl_3$ has a value of approximately 820 – 980 Hv. Therefore, although the Thermo-Calc predictions provided a good estimation, the micro-hardness levels are systematically lower than those found in literature for the $FeAl_3$ IMC - the differences can be associated with the extremely soft Al base material (approximate 30 Hv).

The EBSD maps for the full penetration welds (Fig. 9) show distinct variation in grain size distributions. These distinct microstructures are explained by 2 main factors:

(1) *effect of the cooling rate and thermal gradient from different power ratios* - Sun et al. [40] detailed the effects of the adjustable ring-mode laser on the cooling rates and subsequent grain structure. They noted that the proper core/ring power ratio can restrict the formation of columnar grains near the interface, resulting in grain refinement within the weld zone. Extremely high power ratio, for example the core

beam alone (r = ∞), results in high peak temperature and allows a long time for heat dissipation prior to solidification, leading to low thermal gradient and cooling rate at the solidification front; extremely low power ratio, for example the ring beam alone (r = 0), provides excessive pre-heating and post-heating, mitigating the thermal gradient and slowing down the cooling process. A compromised solution which balances the wider formation of equiaxed dendrites and better grain refinement was determined at r = 0.33. These trends are reflected in the current study, and we observed at r = 0.5 for the full penetration keyhole mode (ID 15/ MR) a significant grain refinement. This is seen through the finer columnar grains in the MR weld (~50 μm in width with r = 5) compared to the coarser columnar grains in the ID 7/ MC and ID 21/ IC welds (~150 μm in width with r = 5 and 1, respectively). For the MC and IC welds a similar microstructure is observed with coarse grains, due to the reduction in the cooling rate. For the MR trial a very fine equiaxed grain structure is observed that cannot be explained only by the high cooling rate. Further discussion via solute effect is deemed necessary.

(2) *solute effect* - The maximum ring power of the MR trial increased the localised heat input in the top sheet of the weld and created a wider molten pool, which can be seen in Figs. 7–8. Further to this, the convective Marangoni flows together with the buoyancy forces acting in the weld pool enable the Al to mix into the upper steel sheet via vortices generated on the sides of the molten pool [45]. The high amount (23 wt%) of Al solute in the Fe-rich region of the

ID 15/ MR weld accumulates ahead of the solid/liquid interface during solidification which reduces the growth velocity during the diffusion-controlled grain growth - this theory is termed the growth restriction effect of solutes [46]. The presence of Al-rich solute creates the transition of a columnar grain structure to a fine equiaxed grain structure through constitutional supercooling, via heterogenous nucleation of grains in Al-rich regions [6]. The overall effect of solute on the grain size reduction is based on a growth restriction factor (*GRF*) or a constitutional supercooling parameter *(P)* [46,47].

5. Conclusions and final remarks

This paper has investigated the impact of the ARM laser on the IMC formation, microstructure and mechanical properties of dissimilar overlap welded joints of IF steel to 1050 aluminium alloy. Findings have been presented by considering three welding modes (conduction mode, keyhole mode in partial and full penetration) and the three selected laser beam shapes (core-dominant beam; ring-dominant beam; intermediate-core beam). It was found that the proper selection of core/ring power ratio is a key parameter to control both IMC formation and microstructure and hence maximise the mechanical properties of the weld. Main conclusions are drawn as follows:

- In conduction mode, the ring-dominant beam (power ratio = 0.2) provided the most optimal weld in terms of strength (71% joint efficiency), whilst limiting metal-mixing. The core beam (at approximate 15% of the total power) allowed for sufficient penetration of the steel and facilitated in the opening of the molten pool; and, the predominant ring beam (at approximate 85% of the total power) was effective in providing a greater lateral heat distribution which increased the surface area of the welded joint. Furthermore, the total IMC thickness as well as the individual Fe_2Al_5 phase was reduced, which was due to the lower peak temperature of the ring-dominant setup and subsequently less melting and mixing of the Fe and Al.
- In keyhole mode (partial and full penetration), the greater weld depth penetration and higher aspect ratio, generated from the core-dominant beam, was however opposed by the significant reduction in weld strength, compared to the conduction mode trials. Notably, the ring-dominant beam (power ratio = 0.5) showed a significant effect of grain refinement in the steel side of the weld. This was due to two main factors: first, the lower peak temperatures from the ring-dominant beam which resulted in a faster cooling rate; and second the migration of Al solute into the upper portion of the weld, which had a growth restriction effect on the grain structure. Strong correlation between the Vickers micro-hardness and Thermo-Calc predictions on the vol% of phases formed was found - greater vol% of Fe_4Al_{13} resulted in greater micro-hardness.

This paper proves the feasibility of controlling IMC phase formation by using ARM laser technology. Results could be helpful in representing the distinctive benefits of the ARM laser to the laser-material processing community and more broadly to design and material engineers. This opens interesting opportunities in the broader area of laser beam shaping as a tool to create bespoke microstructures during the joining of dissimilar materials. Although results are encouraging, compared to a single-beam laser, selecting the optimal set of parameters for a laser beam shaping technology requires significant efforts. In this context, future work will complement experimental studies with advanced multi-physical simulations to better understand the mechanisms behind the material mixing and diffusion processes and provide informa-

tion about temperature fields and fluid flow, all of which are difficult to measure directly via physical experiments.

Data availability

Data will be made available on request.

Declaration of Competing Interest

The authors declare that they have no known competing financial interests or personal relationships that could have appeared to influence the work reported in this paper.

Acknowledgements

References

[1] S. Kuryntsev, A Review: Laser Welding of Dissimilar Materials, Materials (Basel) 15 (122) (2022) 30, https://doi.org/10.3390/ma15010122.

[2] A. Sadeghian, N. Iqbal, "A review on dissimilar laser welding of steel-copper, steel-aluminum, aluminum-copper, and steel-nickel for electric vehicle battery manufacturing," *Opt. Laser Technol.*, vol. 146, no. May 2021, p. 107595, 2022, doi: 10.1016/j.optlastec.2021.107595.

[3] H.K.D.H. Bhadeshia, Problems in the welding of automotive alloys, Sci. Technol. Welding Joining. (2015), https://doi.org/10.1179/15Z.000000000379.

[4] D. Wallerstein et al., Recent developments in laser welding of aluminum alloys to steel, Metals. (2021), https://doi.org/10.3390/met11040622.

[5] H.R. Kotadia, P. Franciosa, D. Ceglarek, Challenges and Opportunities in Remote Laser Welding of Steel to Aluminium, MATEC Web Conf. 269 (2019) 02012, https://doi.org/10.1051/matecconf/201926902012.

[6] H.R. Kotadia, P. Franciosa, S. Jabar, D. Ceglarek, Remote laser welding of Zn coated IF steel and 1050 aluminium alloy: processing, microstructure and mechanical properties, J. Mater. Res. Technol. 19 (2022) 449–465, https://doi.org/10.1016/j.jmrt.2022.05.041.

[7] M. Mohammadpour, N. Yazdian, G. Yang, H.P. Wang, B. Carlson, R. Kovacevic, Effect of dual laser beam on dissimilar welding-brazing of aluminum to galvanized steel, Opt. Laser Technol. 98 (2018) 214–228, https://doi.org/10.1016/j.optlastec.2017.07.035.

[8] S. Deng, R. Yuan, X. Tang, F. Lu, Migration behavior of IMC layer in twin-spot laser welding-brazing of aluminum to steel, Mater. Des. 188 (2020), https://doi.org/10.1016/j.matdes.2020.108489 108489.

[9] D. Narsimhachary, K. Dutta, S. M. Shariff, G. Padmanabham, and A. Basu, "Mechanical and microstructural characterization of laser weld-brazed AA6082-galvanized steel joint," *J. Mater. Process. Technol.*, vol. 263, no. June 2018, pp. 21–32, 2019, doi: 10.1016/j.jmatprotec.2018.08.002.

[10] H. Springer, A. Kostka, E.J. Payton, D. Raabe, A. Kaysser-Pyzalla, G. Eggeler, On the formation and growth of intermetallic phases during interdiffusion between low-carbon steel and aluminum alloys, Acta Mater. (2011), https://doi.org/10.1016/j.actamat.2010.11.023.

[11] L. Cui, B. Chen, W. Qian, D. He, L. Chen, Microstructures and mechanical properties of dissimilar Al/steel butt joints produced by autogenous laser keyhole welding, Metals (Basel) 7 (11) (2017) pp, https://doi.org/10.3390/met7110492.

[12] O. Seffer, R. Pfeifer, A. Springer, S. Kaierle, Investigations on laser beam welding of different dissimilar joints of steel and aluminum alloys for automotive lightweight construction, Phys. Procedia 83 (2016) 383–395, https://doi.org/10.1016/j.phpro.2016.08.040.

[13] J. Ma, M. Harooni, B. Carlson, R. Kovacevic, Dissimilar joining of galvanized high-strength steel to aluminum alloy in a zero-gap lap joint configuration by two-pass laser welding, Mater. Des. 58 (2014) 390–401, https://doi.org/10.1016/j.matdes.2014.01.046.

[14] M.W. Safeen, P.R. Spena, Main issues in quality of friction stir welding joints of aluminum alloy and steel sheets, Metals (Basel) 9 (5) (2019) pp, https://doi.org/10.3390/met9050610.

[15] K.M. Hong, Y.C. Shin, Prospects of laser welding technology in the automotive industry: A review, J. Mater. Process. Technol. 245 (2017) 46–69, https://doi.org/10.1016/j.jmatprotec.2017.02.008.

[16] M. Jarwitz, F. Fetzer, R. Weber, T. Graf, Weld seam geometry and electrical resistance of laser-welded, aluminum-copper dissimilar joints produced with spatial beam oscillation, Metals (Basel) 8 (7) (2018) pp, https://doi.org/10.3390/met8070510.

[17] Y. Meng, M. Gong, S. Zhang, Y. Zhang, M. Gao, Effects of oscillating laser offset on microstructure and properties of dissimilar Al/steel butt-joint, Opt. Lasers Eng. vol. 128, no. January (2020), https://doi.org/10.1016/j.optlaseng.2020.106037 106037.

[18] C. Prieto et al., Dynamic laser beam shaping for laser aluminium welding in e-mobility applications, Procedia CIRP 94 (2020) 596–600, https://doi.org/10.1016/j.procir.2020.09.084.

[19] X. Gao, Z. Li, L. Wang, X. Zhou, D. You, and P. P. Gao, "Detection of weld imperfection in high-power disk laser welding based on association analysis of multi-sensing features," Opt. Laser Technol., vol. 115, no. September 2018, pp. 306–315, 2019, doi: 10.1016/j.optlastec.2019.01.053.

[20] L. Wang et al., Adjustable Ring Mode (ARM) laser welding of stainless steels, Opt. Lasers Eng. 137 (August) (2020) 2021, https://doi.org/10.1016/j.optlaseng.2020.106360.

[21] T. Sun, N. Ferguson, C. Liu, G. Gibbons, and P. Franciosa, "Application of adjustable ring mode laser in remote laser welding of additive manufactured AlSi10Mg alloy Application of adjustable ring mode laser in remote laser welding of additive manufactured AlSi10Mg alloy," vol. 042007, no. June, 2022, doi: 10.2351/7.0000794.

[22] V.V. Pamarthi, T. Sun, A. Das, P. Franciosa, Strain-based investigation on solidification crack susceptibility of 6005 investigation on solidification crack susceptibility of 6005 aluminium using mode (ARM) laser welding, Procedia CIRP 111 (2022) 425–430, https://doi.org/10.1016/j.procir.2022.08.180.

[23] F. Gabler, Lasers lead the charge in e-mobility manufacturing, Ind. Laser Solut. (2019).

[24] A. Haeusler, S. Hollatz, A. Olowinsky, A. Gillner, R. Poprawe, Quality improvement of the surface of laser micro welds by using a dual beam setup, J. Laser Appl. (2018), https://doi.org/10.2351/1.5040626.

[25] M. Mohammadpour, L. Wang, F. Kong, R. Kovacevic, Adjustable ring mode and single beam fiber lasers: A performance comparison, Manuf. Lett. 25 (2020) 50–55, https://doi.org/10.1016/j.mfglet.2020.07.003.

[26] M. Duocastella, C.B. Arnold, Bessel and annular beams for materials processing, Laser Photonics Rev. 6 (5) (2012) 607–621, https://doi.org/10.1002/lpor.201100031.

[27] J. Volpp, F. Vollertsen, "Impact of multi-focus beam shaping on the process stability," Opt. Laser Technol., vol. 112, no. November 2018, pp. 278–283, 2019, doi: 10.1016/j.optlastec.2018.11.032.

[28] K.S. Hansen, M. Kristiansen, F.O. Olsen, Beam shaping to control of weldpool size in width and depth, Phys. Procedia vol. 56, no. C (2014) 467–476, https://doi.org/10.1016/j.phpro.2014.08.150.

[29] R. Yuan, S. Deng, H. Cui, Y. Chen, F. Lu, Interface characterization and mechanical properties of dual beam laser welding-brazing Al/steel dissimilar metals, J. Manuf. Process. 40 (January) (2019) 37–45, https://doi.org/10.1016/j.jmapro.2019.03.005.

[30] S. Yan, Z. Hong, T. Watanabe, T. Jingguo, CW/PW dual-beam YAG laser welding of steel/aluminum alloy sheets, Opt. Lasers Eng. 48 (7–8) (2010) 732–736, https://doi.org/10.1016/j.optlaseng.2010.03.015.

[31] H. Xia, W. Tao, L. Li, C. Tan, K. Zhang, and N. Ma, "Effect of laser beam models on laser welding–brazing Al to steel," Opt. Laser Technol., vol. 122, no. September 2019, p. 105845, 2020, doi: 10.1016/j.optlastec.2019.105845.

[32] G. Chen, B. Wang, S. Mao, P. Zhong, and J. He, "Research on the '∞'-shaped laser scanning welding process for aluminum alloy," Opt. Laser Technol., vol. 115, no. December 2018, pp. 32–41, 2019, doi: 10.1016/j.optlastec.2019.01.046.

[33] O. Seffer, S. Nothdurft, J. Hermsdorf, and S. Kaierle, "Investigations on welding of several materials with adjustable intensity profiles: new approaches and findings," 2020, doi: 10.1117/12.2566034.

[34] M. Rasch et al., "Shaped laser beam profiles for heat conduction welding of aluminium-copper alloys," Opt. Lasers Eng., vol. 115, no. November 2018, pp. 179–189, 2019, doi: 10.1016/j.optlaseng.2018.11.025.

[35] L. Wang et al., Monitoring of keyhole entrance and molten pool with quality analysis during adjustable ring mode laser welding, Appl. Opt. 59 (6) (2020) 1576, https://doi.org/10.1364/ao.383232.

[36] M. Chelladurai Asirvatham, S. Collins, and I. Masters, "Laser wobble welding of steel to Aluminium busbar joints for Li-ion battery packs," Opt. Laser Technol., vol. 151, no. September 2021, p. 108000, 2022, doi: 10.1016/j.optlastec.2022.108000.

[37] T. Sun, P. Franciosa, D. Ceglarek, Effect of focal position offset on joint integrity of AA1050 battery busbar assembly during remote laser welding, J. Mater. Res. Technol. 14 (2021) 2715–2726, https://doi.org/10.1016/j.jmrt.2021.08.002.

[38] BS EN ISO 14273, "Specimen dimensions and procedure for shear testing resistance spot , seam and embossed projection welds," Br. Stand., 2001.

[39] P. Matysik, S. Jóźwiak, T. Czujko, Characterization of low-symmetry structures from phase equilibrium of Fe-Al system-microstructures and mechanical properties, Materials (Basel) 8 (3) (2015) 914–931, https://doi.org/10.3390/ma8030914.

[40] T. Sun, A. Mohan, C. Liu, P. Franciosa, D. Ceglarek, The impact of Adjustable-Ring-Mode (ARM) laser beam on the microstructure and mechanical performance in remote laser welding of high strength aluminium alloys, J. Mater. Res. Technol. 21 (2022) 2247–2261, https://doi.org/10.1016/j.jmrt.2022.10.055.

[41] G. Zhang, M. Chen, Y. Shi, J. Huang, F. Yang, Analysis and modeling of the growth of intermetallic compounds in aluminum-steel joints, RSC Adv. 7 (60) (2017) 37797–37805, https://doi.org/10.1039/c7ra06354g.

[42] J. Yang, Y.L. Li, H. Zhang, Microstructure and mechanical properties of pulsed laser welded Al/steel dissimilar joint, Trans. Nonferrous Met. Soc. China (English Ed. 26 (4) (2016) 994–1002, https://doi.org/10.1016/S1003-6326(16)64196-1.

[43] M.J. Torkamany, S. Tahamtan, J. Sabbaghzadeh, Dissimilar welding of carbon steel to 5754 aluminum alloy by Nd:YAG pulsed laser, Mater. Des. 31 (1) (2010) 458–465, https://doi.org/10.1016/j.matdes.2009.05.046.

[44] G. Chianese, S. Jabar, P. Franciosa, D. Ceglarek, S. Patalano, A multi-physics CFD study on the part-to-part gap during remote laser welding of copper-to-steel battery tab connectors with beam wobbling, Procedia CIRP 111 (2022) 484–489, https://doi.org/10.1016/j.procir.2022.08.075.

[45] W. Huang, H. Wang, T. Rinker, W. Tan, Investigation of metal mixing in laser keyhole welding of dissimilar metals, Mater. Des. 195 (2020), https://doi.org/10.1016/j.matdes.2020.109056 109056.

[46] Z. Fan, F. Gao, Y. Wang, H. Men, and L. Zhou, "Effect of solutes on grain refinement," Prog. Mater. Sci., vol. 123, no. December 2020, p. 100809, 2022, doi: 10.1016/j.pmatsci.2021.100809.

[47] M. H. Khan, A. Das, Z. Li, and H. R. Kotadia, "Effects of Fe, Mn, chemical grain refinement and cooling rate on the evolution of Fe intermetallics in a model 6082 Al-alloy," Intermetallics, vol. 132, no. December 2020, pp. 1–10, 2021, doi: 10.1016/j.intermet.2021.107132.